A NOVEL PROBE FABRICATION PROCESS FOR IMPROVEMENT IN SCANNING NEAR-FIELD OPTICAL MICROSCOPY

EUGENIO CEFALÌ

(Nota presentata dal Socio Ordinario Raffaello Girlanda)

ABSTRACT. The full exploitation of the microscope potentialities as surface science tool on nanometer scale strictly depends on the probe features. Recent developments on fiber probes for Scanning Near Field Optical Microscope are reported. In this frame, new models and prototypes of probes with higher performances in terms of optical power efficiency and polarization selectivity are worked out. A new fabrication method of the probes is settled, based on a chemical etching process, which doubles the aspect ratio of the probe sharpness and improves the optical throughput. Moreover, Finite Domain Time Difference simulation allows the designing of a probe able to act as an evanescent field linear polarizer.

1. Introduction

Scanning Near Field Optical Microscope (SNOM) is a powerful tool for surface science on nanometric scale [1, 2, 3, 4, 5]. It has the uniqueness to combine the potentiality of scanning probe technology with the power of optical microscopy. In such a microscope, a nanoscopic light probe is raster scanned very close to the sample surface allowing the investigation of the optical and morphological properties with a spatial resolution well beyond the diffraction limit [6]. The super-resolution is attained by the highly confined evanescent electromagnetic (em) field emerging by the sub-wavelength probe apex. Pohl and coworkers in the 1984 have achieved 25 nm resolution (corresponding to $\lambda/20$) in the visible range [1], whereas sub-10 nm resolution has been reached by Wickramasinghe group [7]. Many SNOM configurations working at room-temperature as well as at low-temperature can be found in literature [4, 8, 9, 10, 11]. An example of typical SNOM configuration is reported in figure 1. A light beam, of suitable wavelength, is coupled to the probe. The latter is mounted onto a mechanical holder and coarsely approached to the sample surface by a motorized microscrews stage. The specimen is placed on a x-y-z piezo actuator that scans the sample under the tip during the experiment. Regarding the control of the probe-surface distance, it is performed by a tuning fork feedback system [12, 13]: the tip joint together at a tuning fork quartz is put in oscillation horizontally at the resonance frequency [14, 15]. As the tip approaches the surface, shear forces acting between the probe and the sample dampen the amplitude of the probe vibration [16]. As consequence, a piezoelectric potential between the two arms of the tuning fork is produced and used as feedback signal for stabilize the distance and for reconstructing the surface topography. Finally, the light scattered by the interaction of probe with the sample is collected in the far

field, in reflection and/or in transmission, by means of a microscope objective and imaged on a photodetector (e.g. photomultiplier PMT, Avalanche Photodiode APD, etc.).
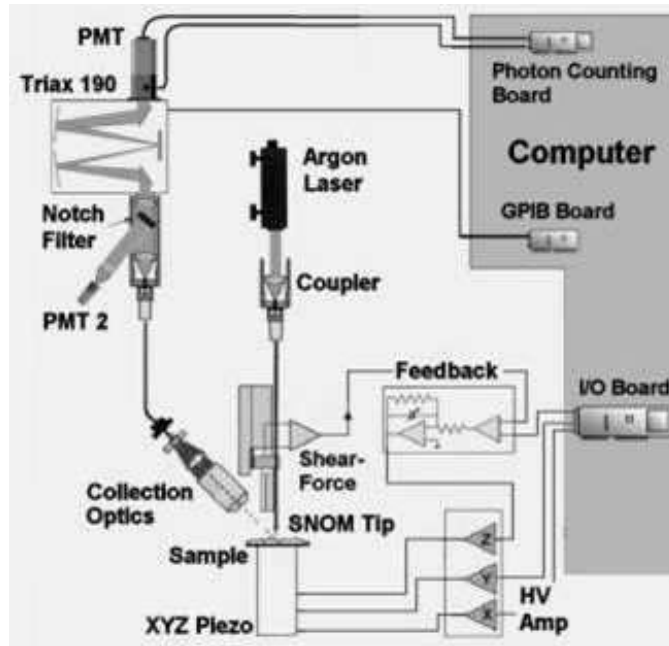
FIGURE 1. Schematic of a typical SNOM setup.

SNOM application ranges almost any science field (physics, chemistry, material and life sciences) [17, 18, 19, 20, 21, 22]. Nevertheless, SNOM potentialities have not been fully exploited yet. It has not been possible to transpose efficiently on nanometer scale all the contrast mechanisms of conventional optical microscopy and spectroscopy (Fluorescence, Raman, Polarization etc.). Analogously to the others scanning probe microscopy (SPM) techniques, such a possibility is strongly dependent on the probe features: it is the key component that determines the SNOM performances. Despite the big efforts devoted for developing SNOM microscopy, improvement of the probes efficiency still remains one of the major challenges. Such an aspect regards both apertureless and aperture probes: metallic and dielectric tips as well as metal coated tapered fiber probes and cantilever hollow [5, 23, 24, 25]. In this frame, the desirable features of a SNOM probe are: i) high optical throughput; ii) small tip aperture or tip apex dimension (at least a few nanometers in diameter); iii) controllable polarization properties. Among several kinds of existing probes the optical fiber one turns out to be the best candidate. It still remains the most commonly used and diffused probe. It has been employed in many SNOM geometries because of its good performances, the relatively easiness of fabrication and its versatility [5, 26, 27]. Apart of the good optical guiding properties (either with continuous or pulsed waves [28, 29], the fiber probe presents good mechanical features in terms of stiffness and high quality factor

as atomic force detector. Therefore, it is also excellent as sensor for the surface topography detection. In this work, recent progresses on the features improvement of the SNOM optical fiber probes are reported. As first result, a new fabrication method of optical fiber probes with high optical throughput is shown. It follows by studies performed on the electromagnetic waves propagation inside the optical fiber probes [30, 31]. Such studies have established that the optical power throughput increases correspondingly with the probe conical angle (i.e. apex aspect ratio). This goal has been reached by an effective modification of an already existing fabrication process called Tube Etching (TE) [32]; it is actually admitted to be the best system for producing SNOM fiber probes. The process consists of chemical attack of the fiber by a hydrofluoric acid bath. In particular, a combination of convective and diffusive fluxes of acid inside the fiber jacket (it acts as a capillary) taper the SiO_2 core until to produce a conical shape apex. The new worked out technique, called Reverse Tube Etching (RTE), consists of in inserting vertically the fiber in the etching bath in upside-down geometry. The method has allowed obtaining optical fibers with a cone angle double respect to the TE technique and consequently an improving of the optical throughput. At the same time, a unique theory able to explain both the TE and the RTE processes has been developed [33]. Moreover, a model of a new aperture probe design, able to produce a well defined near-field polarized light, has been implemented. The idea has consisted to modify the apex part of a SNOM optical fiber probe in order to fabricate a structure that mimics an electric dipole. Such probe behaves as a polarizer: the near field light polarization output is dictated by the tip geometry regardless the polarization state of the incoming light. Properties and performances of the probe have been evaluated by a Finite Domain Time Difference simulation (FDTD). Form the calculus it is turned out that the near field coming out from the probe is linearly polarized. These preliminary results give strictly indications for manufacturing a probe prototype.

2. Theoretical results

SNOM fiber optical probe consists of a cylindrical dielectric waveguide whose apex is tapered and metal coated. The cylindrical part has to guide the coupled light up to the apex with a minimum of losses; whereas the tapered element is the critical mesoscopic transition zone between the macroscopic guide and the apex. It has generally a truncated cone shape, but recently fiber probes with taper zone of trihedral shape have been realised [34]. Such a zone has to be coated with metal layer, basically, to prevent the leakage of light through the sides of the guide, and to create the nanometric aperture. It is a crucial part of the probe. In fact, the optical power efficiency of probe depends strongly on it. While the spatial resolution of the tip and its capability to maintain a well defined light polarization depend on the size and shape of the aperture. In order to go further inside to the probe features, and consequently to their potential improvements, information on the electromagnetic field distribution in front of the probe aperture is required. Due to the complicated boundary conditions imposed by the probe geometry (e.g. truncated conical tip with metal coating), analytical solutions of the Maxwell equations are not available. Consequently, the problem has to be dealt with fully numerical methods (Finite Element Method, Finite Difference Time Domain, Method of Moments) or semianalytical (Method of Multiple MultiPole), which requires extended computational work [35]. Anyway, as first approach,

important information can be achieved by approximating the SNOM aperture probe as a circular hole in an infinite perfectly conducting screen. This is the approximation that Bethe and Bouwkamp have used in their theories [36, 37]. Such an approach is, however, the most extensively diffused in near-field calculations because it leads to the analytical formulae. It consists of solving an electrostatic and magnetostatic eigenvalue problem for the static near field that exists close to the aperture. This solution can be easily recovered by using oblate spheroidal coordinates and harmonical wave functions. In this case, the Helmholtz equation $\left(\left[\nabla^2 + k^2\right] \cdot \varphi(\overrightarrow{r}) = 0\right)$, which reduces to the Laplace equation $\left(\nabla^2 \varphi(\overrightarrow{r}) = 0\right)$, for a hole of small size, has the solution φ as product of parametric Legendre wave functions in spheroidal coordinates. An interesting solution of the equation can be obtained for a metal screen (in the xy plane) containing an aperture of radius r that is irradiated by a plane wave. The radiation of wavelength λ is propagating along the z direction and is polarized along the x-direction. For the electromagnetic field components at the aperture ($r \ll \lambda, z = 0$) (near field components), the following analytical expressions are obtained:

(1)
$$E_x = -\frac{4i\omega E_0}{3\pi c} \cdot \frac{2r^2 - x^2 - 2y^2}{\sqrt{r^2 - x^2 - y^2}}$$

$$E_y = -\frac{4i\omega E_0}{3\pi c} \cdot \frac{x \cdot y}{\sqrt{r^2 - x^2 - y^2}}$$

$$H_z = -\frac{4H_0}{\pi} \cdot \frac{2r^2 - x^2 - 2y^2}{\sqrt{r^2 - x^2 - y^2}}$$

where $E_0 = \left|\overrightarrow{E_0}\right|$ and $H_0 = \left|\overrightarrow{H_0}\right|$ are the amplitudes of the fields and $\overrightarrow{K} = (\overrightarrow{k}, k_z) = (0, k_z)$) is the wave vector ($k = |\overrightarrow{k}| = (\omega/c) = 2\pi/\lambda$). The results of such calculation for the squared components of the electric field [38, 39] are reported in figure 2.
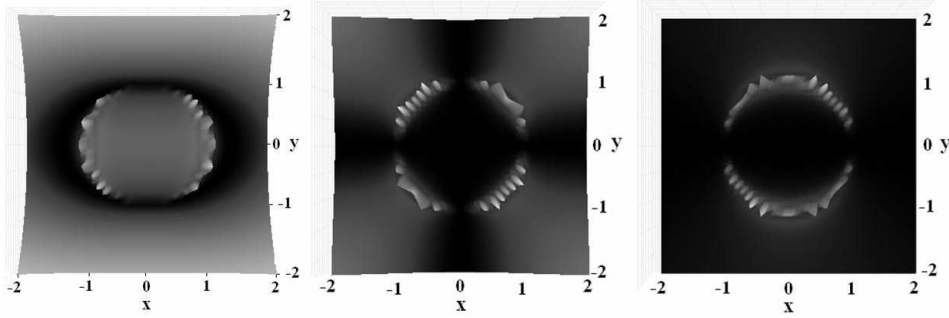
FIGURE 2. Plot of the squared components of the electric field diffracted by a circular aperture in an screen of infinite perfecting conductivity. The plot is performed at z=0 nm into the aperture. (a) and (b) show the $|E_x|^2$ and $|E_y|^2$ respectively, while (c) $|H_z|^2$. The scales on axes are in units of r.

For this calculation an aperture radius of 50 nm and a wavelength of 514 nm has been considered. Observing figure 2 it turns out that the em field is most enhanced near the sharp edge of the aperture: the fields show divergences at the aperture rims. The outcomes above reported confirm that the light is confined around the aperture by whose follows the subdiffraction resolution. Moreover, in literature it is reported that close to the aperture all polarization components of the light are present [38]. Specifically, z-polarized and x-y polarized light exist under the metal forming the aperture. The component in the y-direction has a magnitude much smaller than the others, while far from the aperture the diffracted light will be predominantly x-polarized [38, 40]. Thus, it follows that a circular aperture sustains substantially the polarization components of the incident field [38, 40]. Anyhow, as previously cited, the Bethe-Bouwkamp theory gives exact information on the near field distribution behind an ideal circular aperture. Nevertheless, this theory is useful to gain general information describing an aperture probe (e.g. an optical fiber) if appropriate corrections are applied. In this sense, the field of the ideal aperture presents a singularity at the edges in the plane of polarization and zero value along the other axis outside the aperture. This is not the case for an aperture probe with a metal coating of finite conductivity. At optical frequency's, the shortest skin depths for a metal is of about 6 - 10 nm, which will widen the effective aperture size and smooth out the singular fields at the edges. Moreover, any real metal screen will have a thickness of at least 50-100 nm to attenuate the fields in the lateral direction [41]. Regarding the optical power throughput, a detailed study has been performed by Novotny et al. [30] focused on the propagation of the optical modes in the tapered zone. It revealed that the mode structure in a metallized tapered hollow waveguide changes as a function of the dimension of the dielectric core [30]. Significant simulation has been performed on a discrete model that has considered the cone as a succession of disks with decreasing diameters and infinitesimal thicknesses (fig. 3 [4]). It
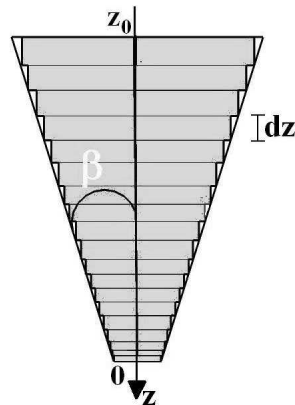
FIGURE 3. Model of the taper zone of a dielectric aperture probe for the calculation of the transmission power.

is pointed out that in the straight dielectric core the guided HE_{11} modes run into cut off one after the other as the diameter decreases on approaching the apex [31]. For diameters smaller of about half wavelength, the energy in the core decays exponentially towards the

apex. It occurs because the propagation constants of all modes become purely imaginary [5, 30]. Thus, it shows that the mode cut off is responsible for the low power throughput of aperture probes as schematized in figure 4.

Moreover, approximately 30% of the guided light is reflected and the metal coating absorbs 70%. Based on this model (see figure 3), it is turned out the following expression for the power loss in the waveguide [4]:

$$(2) \qquad\qquad P_{loss}(z) = P(z_0) \cdot \exp\left[-2\int_{z_0}^{z}\delta_{11}(z)dz\right]$$

$P(z_0)$ is the incident power, whereas $\delta_{11}(z)$ is the attenuation constant of the HE_{11} mode in the z position of the waveguide section. The coefficient δ_{11} depends on the diameter of the waveguide section, on the wavelength, and on the materials properties, respectively. Expressing the power as function of the core diameter d and of half-cone angle β useful information for the probe optimization can be obtained. For an aperture with a coating of infinite thickness, and a z_0 value in the evanescent zone of the HE_{11} mode, the coefficient $\delta_{11}(z)$ is an exponential function

$$(3) \qquad\qquad \delta_{11}(d) = Im(n_{metal} \cdot k_0 e^{-Ad}),$$

n_{metal} is the refraction index of the metal coating, $k_0 = 2\pi/\lambda$ is the free space propagation vector, A is a constant depending on the characteristics of the apex [4]. Entering the $\delta_{11}(d)$ in the equation for $P(z)$ and performing the integration we obtain

$$(4) \qquad\qquad P_{loss}(z) = P(z_0) \cdot \exp\left[a - be^{2Az\tan\beta}\right],$$

in which a and b are two constants depending on n_{metal}, k_0 and d_0 (core diameter). From this expression it follows that the ratio between the input and output power is $P_{out}/P_{in} \propto e^{B \cdot ctg\beta}$ (B is a constant). It clearly shows that the transmission power increases with the cone angle β. Hence the first important result is shown: for a metal coated fiber probe the larger the tapering angle and the higher the power throughput.
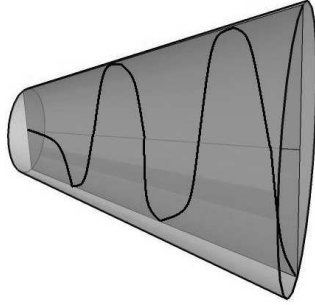
FIGURE 4. Schematic draw of the cut-off of the guided modes into the taper zone of a metal coated probe. To be noted the creation of evanescent wave also inside the probe.

In order to acquire further and more accurate information for realizing a probe proto-type, it has been used a FDTD method: the numerical procedure allows observing the field distribution behind the aperture of a three dimensional optical fiber probe model. For this purpose, the issue has been better addressed in the reciprocal Fourier space (domain of spa-tial frequencies). Figure 5 shows the results of a FDTD simulation performed on a probe having a cone angle of 20, with an aperture diameter of 100 nm and coated with 50 nm aluminum layer. The spectrum of the electric field (amplitude) is computed in near field on a plane at $z = 25nm$ away from the probe aperture. The scale on the x and y axis is the product of the spatial frequency (defined as $f_x = (2\Delta x)^{-1}$ and $f_y = (2\Delta y)^{-1}$) times the radiation wavelength. In this reduced system of coordinates, $|1| = x$ and $|1| = y$ are equal to $\lambda/2$, therefore the subwavelength components lie outside the interval ± 1.
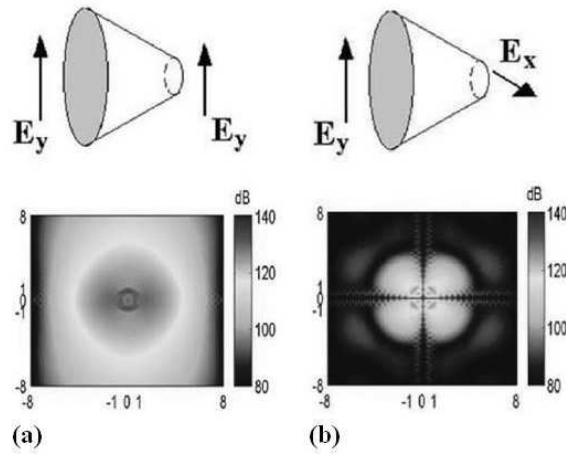
FIGURE 5. Spectrum of electric field (in dB) on a xy plane at $z = 25nm$ away from the probe aperture. (a) It is the angular spectrum obtained feeding the probe with E_y component of the field and calculating the E_y distribution. (b) It is the angular spectrum obtained feeding the probe with E_y component of the field and calculating the E_x distribution The propagative components of the electric field lie between -1 and 1; while the remaining part accounts for the evanescent region of the spectrum. [42]

In this reduced system of coordinates, $x = |1|$ and $y = |1|$ are equal to $\lambda/2$, and there-fore the subwavelength components lie outside the interval ± 1. The probe is fed with a radiation polarized first along y and then along x; whereas the output fields are calculated in both polarization directions y and x. Figures 5a and 5b display the angular spectrum feed-ing the probe with the E_y component of the electric field. The spectra show an isotropic distribution of the Ey components (fig. 5a) and a narrow spectrum of the E_x component (fig 5b), respectively. In particular, the E_x evanescent components have low amplitude. Because of the structure symmetry, the spectrum obtained feeding the probe with the E_x

component would show the same result in the opposite direction. From the calculus it turns out: i) the clear presence of the evanescent components responsible of the subwavelength resolution and the presence of the far field components; ii) the circular aperture is able to maintain the same polarization state of that of the guided light, but it is not able to select one. Moreover, studies on the influence of metal roughness on the near-field distribution at the aperture (roughness magnitude, aperture form) have shown that a dramatic impact exists on the emission characteristics of a near-field probe, and in particular on its polarization sensitivity [43]. Further simulations have been carried out to check new probe models possessing higher optical efficiency and polarization selectivity. The idea comes up from the electromagnetic theory of waveguide in the radio frequency: it has been shown that a coaxial structure has no cut-off frequency and has a power transmission close to unity [44, 45]. In figure 6 an example of the investigated probe is reported. This structure is realised by depositing two separated metal strips instead of the full metal coating in the tapered zone of the fiber. From electromagnetic point of view the probe represents a double connected structure that admits as solution of the Laplace equation ($\nabla_T^2 \psi(x,y) = 0$) wave modes with no cut-off: Transverse Electromagnetic Modes (TEM). For this reason and for the geometry of the taper zone, the probe mimics an electric dipole able to efficiently drive a TEM mode until to the end.
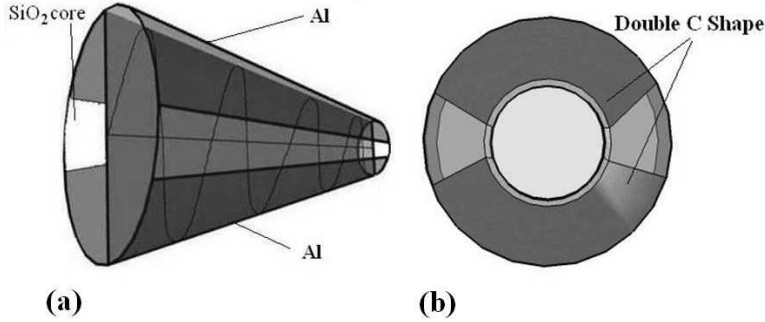
FIGURE 6. Sketch of a Double C shaped optical fiber probe. (a) Side view shows as, in principle, the HE_{11} mode coupled to the fiber is propagating without cut-off. (b) Front view evidence the double C geometry.

For the simulation a structure with a conical angle of 20 has been considered; whereas, the core was coated with two metal slabs (aluminium layer of 50 nm thickness) that realize the Double C structure (fig. 6). Finally, the structure has been completed as a standard probe by depositing uniformly on all the sides a dielectric layer (LiF layer of 25 nm thickness) and finally an aluminum layer of $50nm$ thickness. The results of the simulation are reported in figure 7. The angular spectra obtained by feeding the Double C-shaped probe with E_y are reported in fig 7a and fig. 7c. In particular, the figures show the amplitude of the electromagnetic field components E_y and E_x in the x and y direction, respectively. While, fig. 7b and fig. 7d report the amplitude spectrum of the components E_y and E_x, respectively, calculated feeding the structure by E_x. In figure 7a it is manifest that the propagating field has higher amplitude than the evanescent one. The spectrum has two
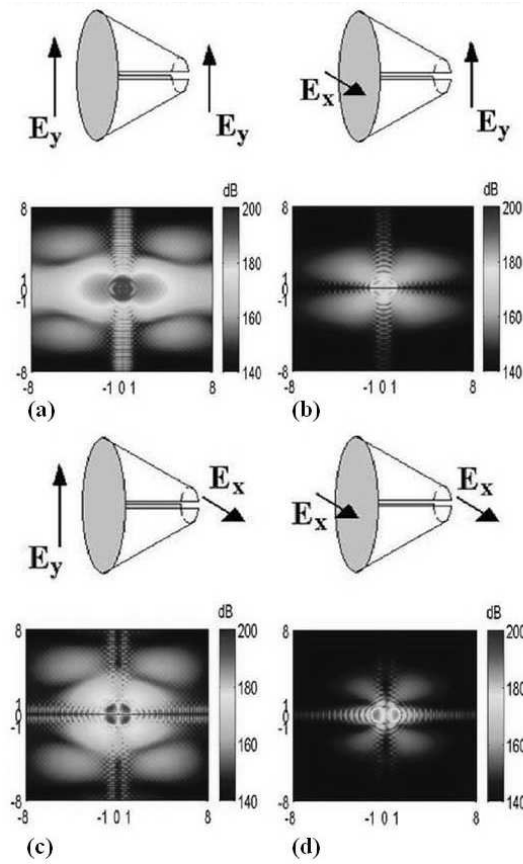
FIGURE 7. Here are reported the Fourier spectra of the Electric field amplitude (E_x and E_y) of the Double C Probe (in dB) on a xy plane at $z = 25nm$ away from the aperture. In the first column the probe is fed with E_y component of the field, whereas in the second column is fed with E_x, respectively. The propagative components of the electric field are between -1 and 1, the remaining part accounts for the evanescent region of the spectrum. Comparing this result with those reported in figure 5 it turns out clearly that such a probe has a power improvement of about $60dB$. However, it has to be stressed that the improvement lies in the far field part of the spectra. [42]

lobes with higher amplitude in the x direction indicating a strong confinement of the field in the x direction of the aperture. Conversely, the polarization of the evanescent field is mostly along the y-axis of the Double C. In figure 7c, the spectrum has on average lower amplitude. In particular, the evanescent components are almost negligible, and therefore the probe allows a low coupling in the direction crossed respect to the y axes of Double

C structure. The structure efficiently couples only the input E_y mode. The narrow distribution and very low amplitude of the spectra reported in figures 7b and 7d show that, for input components of the electric field orthogonal to the Double C structure (x direction), the output is very low and the evanescent components are a few. This simulation indicates that the Double C structure provides a general improvement on power magnitude of the overall angular spectrum and it is able to select a well defined state of polarization. This was the expected result since a double connected structure drives a TEM mode with no cut-off frequency until the end of the probe. However, the probe is not suitable for near-field microscopy: the increased power does not lie in evanescent field, but, conversely, lies in the propagating components.

To overcome these limits, an alternative polarizing aperture SNOM probe is proposed: the "*short-cut Double C*" structure (fig. 8). According to sketch, it is supposed that the polarization state is defined by the Double C topology, while the short conical waveguide attenuates the radiating part of the field maintaining alive the evanescent components. Of course, the shorter the cone, the higher the near field amplitude. By this arrangement the TEM mode is driven very close to the end of the probe without cut-off. The angular spectrum of the electric field amplitude of this new structure is presented in fig. 9. The first row (fig. 9a and fig. 9b) shows the E_y spectrum obtained feeding the short-cut Double C structure with E_y and E_x respectively. The second row (fig. 9c and fig. 9d) displays the amplitude of the E_x components obtained by feeding the probe again with E_x and E_y.
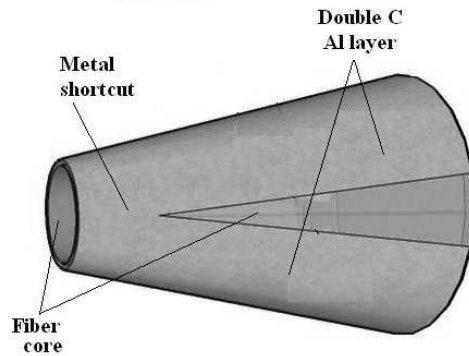
FIGURE 8. Sketch of the Short-cut Double C probe.

We can observe that, feeding the structure along the y axis and along the x axis of the structure, the spectra are pretty similar but attenuated one respect to the other. Such spectra are different from those calculated for the pure Double C. Indeed, in this case, independently on the direction of the fed component of the electric field, the output spectra have the same distribution of spatial frequencies along y and x, respectively, corresponding to an aperture field well confined in both the dimensions. In particular, the spectra in figs. 9a,b have an isotropic distribution of components as for the standard probe.

The spectra calculated in a direction orthogonal to the Double C structure, (i.e. x), present much lower amplitude and a narrow distribution concentrated around the propagating zone. Thus the ratio between the near field and the far field component is improved
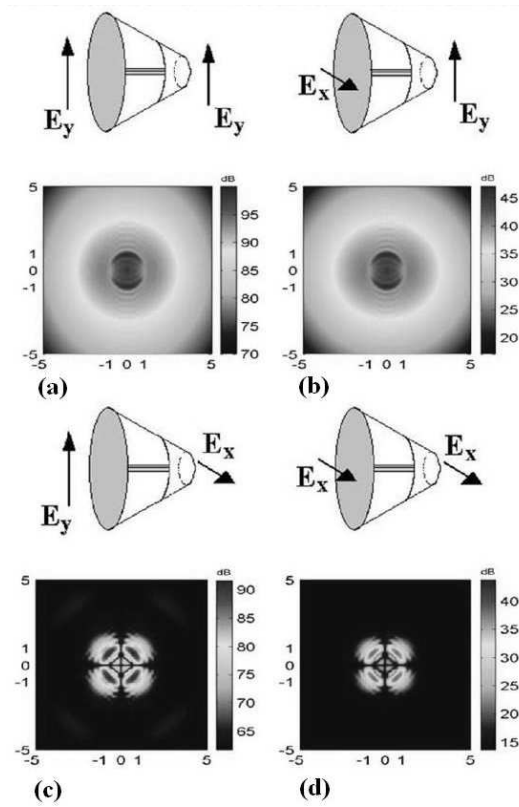
FIGURE 9. Spectrum of electric field (in dB), on a xy plane at 25 nm from the probe aperture, for the Short-cut Double C structure of fig. 8. On the first [second] row the calculated E_y [E_x] component is shown. In the first and second column, the Double C probe is fed with the E_y and E_x, respectively. The radiative region of the electric field is between -1 and 1, the remaining part accounts for evanescent the region of the spectrum. [42]

because most of the amplitude is distributed on the evanescent components (figs. 9a,b). Such result confirms that the *short-cut double C* probe acts as polarizer producing a near field light linearly polarized regardless the polarization state of the light coupled into the fiber. Based on the simulation results, important indications for the realization of a probe prototype arise.

3. Experimental results

Based on the theoretical results above treated, an experimental study, aimed to produce optical fiber probes with a high optical efficiency of transmission, has been performed. In this sense, the Reverse Tube Etching technique has been implemented. The novel method is

a modification of the normal tube etching. It consists of immerging the fiber in hydrofluoric acid and chemically etched in an upside-down geometry. The tip so realized is expected to have a higher conical angle and consequently a higher optical throughput. In order to test the process feature and its reliability, two groups of ten fibers have been manufactured by TE and by RTE, respectively. In particular, for the study multimode optical fibers ($3M$, FT-200-UMT) have been used, with a 200 m core diameter, a hard polymer cladding ($TECS$ ©) of 250 m diameter and a jacket of 500 m diameter [33]. This double work is required because both the cone angle and the roughness of the surface depend on the acid concentration, on the process temperature and on the fiber material [32]. Two groups of fibers, treated in the same experimental conditions, give a precise idea of the process efficiency. Figure 10a shows the optical image of a typical tip obtained in the normal TE. It has a regular surface and a cone angle of about 15 degrees. The same surface quality is

(a)   (b)
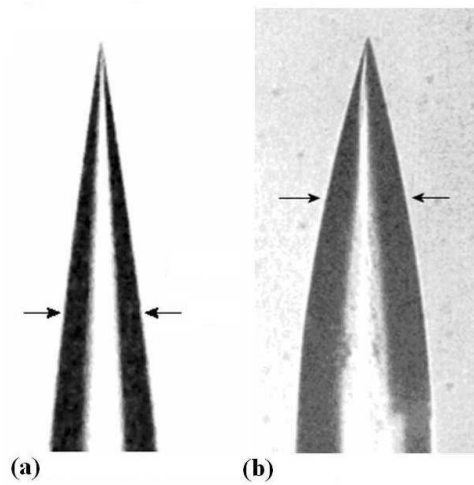
FIGURE 10. Optical images of SNOM probes produced by TE (a) and by RTE (b) in the same experimental conditions. The arrows indicate two zones of 100 μm width.

obtained in the RTE, as shown in fig. 10b. Here the cone angle is remarkably wider of about 25 degrees. To explain this result, it is useful to take in account the model used by Stöckle et al. [32] for describing the TE process: the model of the chemical etching is based on a combination of convective and diffusive processes occurring inside the jacket. By starting from their considerations and from the above founded experimental results, a simple model is here proposed that takes into account the gravity forces to explain the increase of the cone angle in the RTE. The presence of a stationary gravitational field in a liquid mixture induces a concentration gradient leading to a mass flux named barodiffusion [46]. In the TE process the acid convective flux that attacks the core surface is resolved into a radial component J_{Nrconv} and a vertical component J_{Nzconv}. Such vectorial decomposition is justified as long as the chemical etching remains a linear process. Since it has been observed that the final effect of the etching is approximately linear, as proved by the probe surface shape

of figs. 10a and 10b, the causes must be linear too, according to the Curie Principle. As reported into ref. [32], at the core-acid interface the following chemical reactions take place:

$$SiO_2 + 4HF \quad \rightarrow \quad SiF_4 + 2H_2O$$
$$(5) \qquad\qquad 3SiF_4 + 2H_2O \quad \rightarrow \quad 3SiO_2 + 2H_2SiF_6.$$
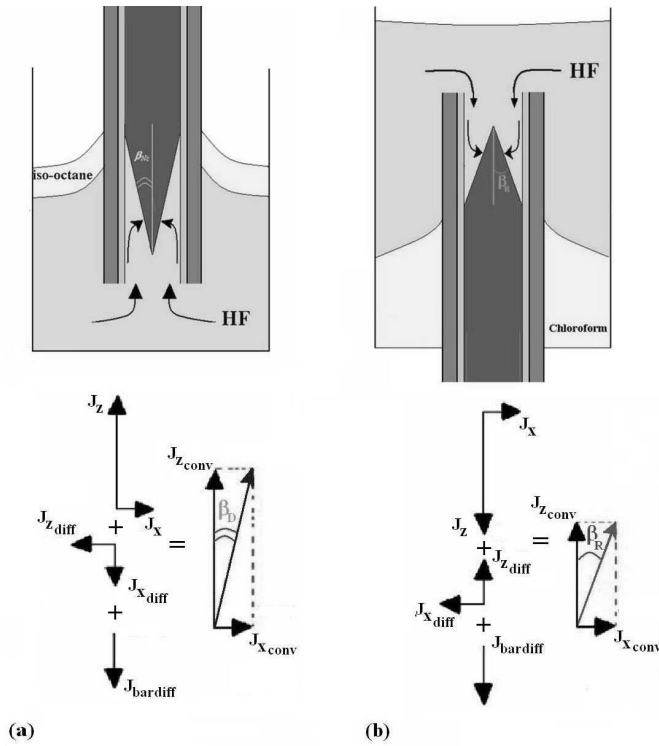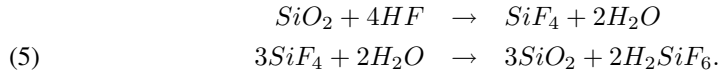
FIGURE 11. Schematic diagram of the experiment for TE (a), and for RTE (b). The vectorial diagrams describe the fluxes in the two experimental geometries.

Hence, as shown in fig. 11a, spatial gradient and an exit flux are generated. The fluxes generated inside the capillary tube are mainly due to a diffusive component and a convective one [32]. Furthermore, to take in account the effects of the gravity, a component $J_{bardiff}$ due to a barodiffusion has to be added. The barodiffusion part has the following expression [46]:

$$(6) \qquad\qquad J_{bardiff} = \rho D \cdot \frac{k_p}{p_I} \cdot \nabla p,$$

where ρ is the mass density of the product, D is the mutual diffusion coefficient, k_p is the barodiffusion ratio, p_I is the hydrostatic pressure inside the capillary (mainly due to the hydrofluoric acid), and ∇p is the pressure gradient containing the gravity force. By considering as positive the direction of entering fluxes, from the chemical-physical point of view, an effective convection flux along z ($J_{Nzconv}(E_f)$), and along r ($J_{Nrconv}(E_f)$) are defined. These represent the amount of acid that effectively etches the fiber core per second. The role of the diffusive components along z, r and of the barodiffusive component along z is to remove the reaction products on the attacked core surface. The main effect of the diffusive components is to allow the incoming of fresh acid on the core surface not yet etched. Thus, the acid fluxes, which effectively etch the core, have a reversed sign with respect to the diffusive and barodiffusive fluxes that generated them. The following equations hold:

$$\begin{aligned}
\vec{J}_{Nzconv}(E_f) &= \vec{J}_{Nzconv} + \vec{J}_{zdiff} + \vec{J}_{bardiff} \\
\vec{J}_{Nrconv}(E_f) &= \vec{J}_{Nrconv} + \vec{J}_{rdiff} \, .
\end{aligned}$$

(7)

$\vec{J}_{Nzconv}$ and $\vec{J}_{Nrconv}$ are the convective acid fluxes along the z and the radial direction; $\vec{J}_{zdiff}$ and $\vec{J}_{rdiff}$, are the acid fluxes along z and the radial direction due to the diffusive processes of the reaction products.

Due to the cladding-core discontinuity and to a better *wettability* of the cladding surface, the acid etching is more favourite along the fiber walls than to centre ($J_{Nzconv} > J_{Nrconv}$), i.e. the etching starts from the fibers walls and proceeds toward the centre. In terms of rates etching (i.e. quantity of core etched per second), this means that the rate along z, $a_{N_z} = dz/dt$, and the rate along r, $a_{N_r} = dr/dt$, are not the same, being $a_{N_z} > a_{N_r}$. The tip will be completed at the time t_s, when the etching along r reaches the centre of the fiber: $t_s = d/2a_r$. Within this time interval the etching along z reaches the quote $z_s = a_z t_s$, producing a conical shape of the fiber edge. The cone angle β_N depends on the etching rates along r and z as follows:

$$\tan \frac{\beta_N}{2} = \frac{r_s}{z_s} = \frac{a_{Nr}}{a_{Nz}}.$$

(8)

This simple model is able to explain why the TE is a self-limiting process [32, 33], i.e. the pencil shape of the fiber obtained at the time t_s is not affected by the acid etching occurring for a time longer than ts. The equation for the half shape of the probe at time t_s into the plane $r - z$:

$$z(r, t_s) = z_s - \frac{1}{\tan \frac{\beta_N}{2}} \cdot r,$$

(9)

holds for every time $t > t_s$ (Fig. 12), since every point of the core profile is etched of the quantity a_z along z and a_r along r, the cone height z is kept constant at the value z_s. The height increase along the core sides ($a_z \cdot t$) is compensated by the height reduction in the centre of the core ($-(\frac{a_r}{\tan(\beta_N/2)} \cdot t)$). The geometry of the cone shape is unaffected, the only effect of the etching for $t > t_s$ being the translation of the cone in the up direction (Fig.12).
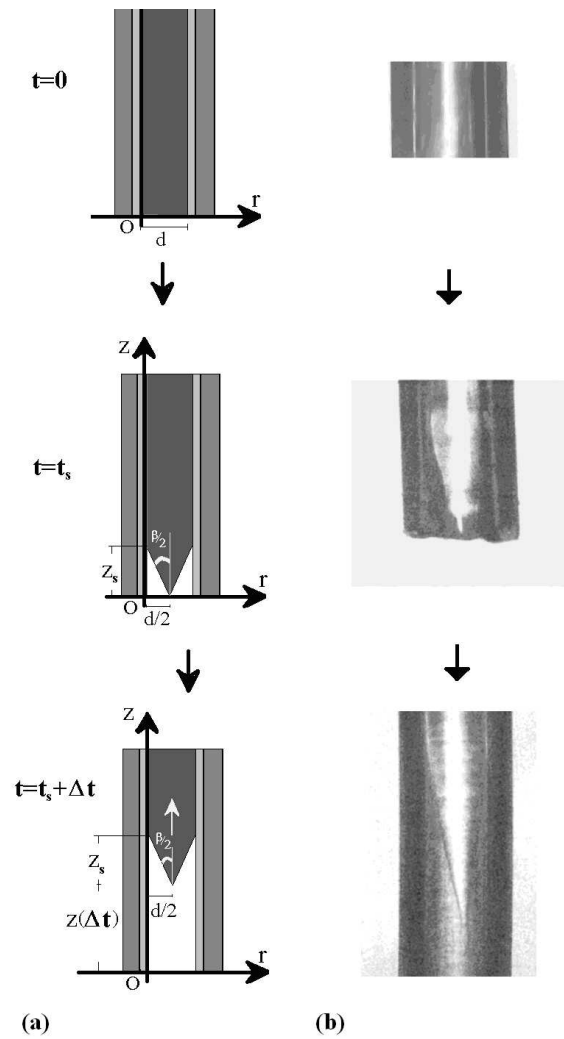
FIGURE 12. Time evolution of the fiber shape as given by the model (a) and by the experiment (b).

The RTE can also be modelled by equations (7), provided the sign of the barodiffusion component is reversed: in this frame, the direction of the gravity force is opposite to the diffusive flux and to the convective flux directions. Hence, choosing again as positive the entering tube direction, the effective convection fluxes along the z and r directions become:

$$\vec{J}_{Rzconv}\left(E_f\right) = \vec{J}_{Rzconv} + \vec{J}_{zdiff} - \vec{J}_{bardiff}$$

(10)
$$\vec{J}_{Rrconv}\left(E_f\right) = \vec{J}_{Rrconv} + \vec{J}_{rdiff}\,.$$

$J_{Rz_{conv}}$ and $J_{Rr_{conv}}$ are the convective acid fluxes along the z and the radial direction r in the reverse frame; $J_{z_{diff}}$ and $J_{r_{diff}}$, are the fictitious acid fluxes along z and the radial direction due to the diffusive process of the reaction products. Equations (7,8,10) clarify the working principle for the new settled method. The barodiffusion in the reversed geometry decreases the convective flux component along the z axis and increases the tip angle. For lower z component of the flux, the etching rate decreases in the same direction as

(11)
$$\tan\frac{\beta_R}{2} = \frac{a_{Rr}}{a_{Rz}} > \frac{a_{Nr}}{a_{Nz}} = \tan\frac{\beta_N}{2},$$

and the cone angle obtainable by RTE is higher than that obtainable by TE ($\beta_R > \beta_N$) (Fig. 11). As an example of the results achievable by this procedure, figure 13 shows the optical image of a typical reversely tube etched tip, characterized by a cone angle of about 30 degrees.
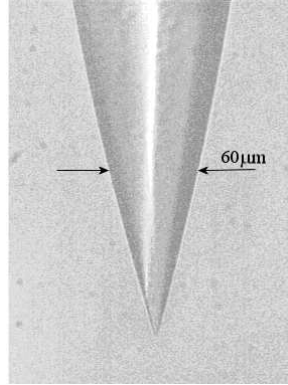
FIGURE 13. Optical image of a reversely etched SNOM probe with a cone angle of about 30 degrees.

4. Conclusions

The development of new models and prototype of aperture SNOM probes manifesting higher optical efficiency is reported. In particular, a new process for probes fabrication, named Reverse Tube Etching, is illustrated. The method guarantees a wider angle of the probe compared to the normal etching results. This improvement, explained by the same model describing the Tube Etching process, is ascribed to the weakening of the effective z component of the etching flux induced by the barodiffusion. The method, easy and reliable, gives a sizeable contribution in upgrading the low-cost production of single step etching

of high throughput near-field probes. The modeling of a novel aperture SNOM probe, able to select a well defined polarization state, is further presented. This probe, named shortcut double C probe, consists of a two-conductors joint at the apex into a small single-conductor waveguide. Numerical FDTD simulations confirm that the near field spectrum is qualitatively independent on the polarization state of the incoming light and that the electromagnetic field emerging from the probe aperture has a well defined linear polarization. Finally, on the basis of the simulation results accurate suggestions for the fabrication of a probe prototype are given.

References

[1] DW. Pohl, W. Denk, M. Lanz *Appl. Phys. Lett.* **44**, 651 (1984)

[2] A. Lewis, M. Isaacson, A. Harootunian, A. Muray *Ultramicrosc.* **13**, 227 (1984)

[3] M. De Serio, R. Zenobi, V. Deckert *Trends in Analytical Chemistry* **22**, 70 (2003)

[4] L. Novotny and B. Hecht *Principles of Nano-Optics* (Cambridge Univ Press, Cambridge, UK, 2006)

[5] B. Hecht, B. Sick, UP. Wild, V. Deckert, RM. Zenobi, OJF. Martin, DW. Pohl *J. Chem. Phys.* **112**, 7761 (2000)

[6] M. Abbe *Archiv Mikroscop Anat Entwicklungsmech* **9**, 413 (1873)

[7] F. Zenhausern, Y. Martin, H. Wickramasinghe *Science* **269**, 1083(1995)

[8] RD. Grober, TD. Harris, JK. Trautman, E. Betzig*Rev Sci Instrum* **65**, 626 (1994)

[9] Y. Durand, JC. Woehl, B. Viellerobe, W. Gohde, M. Orrit *Rev Sci Instrum* **70**, 1318 (1999)

[10] MH. Gray, JWP. Hsu *Rev Sci Instrum* **70**, 3355 (1999)

[11] E. Cefalì, S. Patané, PG. Gucciardi, M. Labardi, M. Allegrini *J Of Microscopy* **210**, 262 (2003)

[12] K. Karrai, RD. Grober *Ultramicroscopy* **61**, 197 (1995)

[13] A. Ambrosio A, E. Cefalì, S. Spadaro, S. Patané, M. Allegrini, D. Albert, E. Oesterschulze *Appl Phis Lett* **89**,163108 (2006)

[14] R. Toledo-Crow, P. Yang, Y. Chen, M. Vaez-Iravani *Appl. Phys. Lett.* **60**, 2957 (1992)

[15] E. Betzig, P. Finn, S. Weiner *Appl. Phys. Lett.* **60**, 2484 (1992)

[16] C. Durkan, IV. Shvets *79* **J Appl Phys**, 1219 (1996)

[17] M. Lomascolo, A. Vergine, TL. Johal, R. Rinaldi, A. Passaseo, R. Cingolani, S. Patané, M. Labardi, M. Allegrini, F. Troiani, E. Molinari *Phys Rev B* **66**, 041302 (2002)

[18] A. Ambrosio, M. Alderighi, M. Labardi, L. Pardi, F. Fuso, M. Allegrini *Nanotechnology* **15**, S270 (2004)

[19] S. Patané, PG. Gucciardi, M. Labardi, M. Allegrini *Riv. del Nuovo Cimento* **27**, 1 (2004)

[20] E. Cefalì, S. Patané, A. Arena, G. Saitta, S. Guglielmino, S. Cappello, M. Nicol, M. Allegrini *Scanning* **24**, 274 (2002)

[21] M. Labardi, N Copped, L. Pardi, M. Allegrini, M. Giordano, S. Patané, A. Arena, E. Cefalì *Mol Cryst Liq Cryst* **398**, 33 (2003)

[22] L. Monsú, M. Castriciano, A. Romeo, S. Patané, E. Cefalì, M. Allegrini *J of Phys Chem B* **106**, 2453 (2002)

[23] RC. Jin, YW Chao, CA Mirkin, KL Kelly, GC Schatz, JG Zheng *Science* **294**, 1901 (2001)

[24] J. Michaelis, C. Hettich, A. Zayats, B. Eiermann, J. Mlynek, V. Sandoghdar *Opt. Lett.* **24**, 581 (1999)

[25] E. Oesterschulze, G. Georgiev, M. Muller-Wiegand, A. Vollkopf, O. Rudow *J Of Microscopy* **202**, 39 (2001)

[26] AJ. Meixner, MA. Bopp, G. Tarrach *Appl Opt* **33**, 7995 (1994)

[27] R. Muller, C. Lienau *J of Microscopy* **202** , 339 (2001)

[28] S. Smith, B. Orr, R. Koppelman, T. Norris *CLEO Anaheim MD Technical Dig. Ser.* **8**, 147 (1994)

[29] S. Smith, B. Orr, G. Parent, D. Van Labeke, FI. Baida*J Of Micr.* **202**, 296 (2001)

[30] L. Novotny, C. Hafner *Phys Rev E* **50**, 4094 (1994)

[31] L. Novotny, DW. Pohl, B. Hecht *Ultramicr.* **61**, 1 (1995)

[32] R. Stockle, C. Fokas, V. Deckert, R. Zenobi, B. Sick, B. Hecht, UP. Wild *Appl Phys Lett* **75**, 160 (1999)

[33] S. Patané, E. Cefalì,A. Arena, PG. Gucciardi, M. Allegrini *Ultramicroscopy* **106**, 475 (2006)

[34] M. Spajer, G. Parent, C. Bainier, D. Charraut *J. of Microscopy* **202**, 45 (2001)

[35] C. Girard *Reg. Prog. Phys.* **68**, 1883 (2001)

[36] H. Bethe *Phys Rev* **66**, 163 (1944)

[37] C. Bouwkamp *Philips Res Rep* **5**, 321 (1950)

[38] HD. Hallen, CL. Jahncke *J Raman Spectrosc* **34**, 655 (2003)

[39] HD Hallen, EJ. Ayars, CL. Jahncke *J Micros.* **210**, 252 (2003)

[40] Drezet A, Woehl JC, Huant S *Phys Rev E* **65**, 046611 (2002)

[41] L. Novotny, DW. Pohl *Light propagation in scanning near-field optical microscopy, in: Photons and Local Probes, Eds O. Marti, R. Muller, NATO ASI Series E , Kluwer, Dordrecht,1995)*

[42] S. Patané, E. Cefalì, S. Spadaro, R: Gardelli, M. ALbani, M. Allegrini *J of Microsc* **229**, 183 (2008)

[43] OJF. Martin, M. Paulus *J of Microsc* **205**, 147 (2002)

[44] F. Demming, J. Jersch, S. Klein, K. Dickmann *J. Of Microsc* **201** 383, (2001)

[45] AS. Lapchuk, AA. Kryuchyn *Ultramicroscopy* **99**, 143 (2004)

[46] LD. Landau, EM. Lifshitz *Fluid Mechanics 2nd ed.* (Pergamon, Oxford, 1987)

Eugenio Cefalì
Università degli Studi di Messina
Dipartimento di Fisica della Materia
e Tecnologie Fisiche Avanzate
Salita Sperone, 31
98166 Messina, Italy
E-mail: eugenio.cefali@ortica.unime.it